

## Hydrophobization of up-conversion luminescent films based on nanocellulose/MF<sub>2</sub>:Ho particles (M = Sr, Ca) by acrylic resin

A. A. Luginina<sup>1</sup>, S. V. Kuznetsov<sup>1</sup>, V. V. Voronov<sup>1</sup>, A. D. Yapryntsev<sup>2</sup>, V. K. Ivanov<sup>2</sup>, D. I. Petukhov<sup>3</sup>, A. A. Lyapin<sup>4</sup>, A. S. Ermakov<sup>4</sup>, D. V. Pominova<sup>1</sup>, E. V. Chernova<sup>1</sup>, A. A. Pynenkov<sup>4</sup>, K. N. Nishchev<sup>4</sup>, P. P. Fedorov<sup>1</sup>

<sup>1</sup>Prokhorov General Physics Institute of the Russian Academy of Sciences, Vavilov str. 38, Moscow, 119991, Russia

<sup>2</sup>Kurnakov Institute of General and Inorganic Chemistry of the Russian Academy of Sciences, Leninskii prosp. 31, Moscow, 119991, Russia

<sup>3</sup>Lomonosov Moscow State University, Chemical department, Leninskie Gory str. 1, Moscow, 119991, Russia

<sup>4</sup>Ogarev Mordovia State University, Bolshevistskaya str. 68, Saransk, 430005, Russia

ppfedorov@yandex.ru

DOI 10.17586/2220-8054-2019-10-5-585-598

Luminescent hydrophobic composite films based on nanocrystalline (CNC) and nanofibrillated (CNF) cellulose matrix with up-conversion MF<sub>2</sub>:Ho (M = Ca, Sr) particles and acrylic resin (ACR) as a coating have been synthesized. Flexible, translucent composite films were obtained by molding from the CNC/CNF suspensions with up-conversion particles. ACR coating was applied to the composite film by spraying. Studies have shown that ACR coating with a layer thickness of 7 – 10 μm provides hydrophobic properties for the films, increasing the water contact angle up to 100 ± 2° with a simultaneous improvement in the luminescent properties. Transparency of CNC/CNF/MF<sub>2</sub>:Ho-ACR films in the visible and near IR region improves by 20 – 25 % without compromising the flexibility and thermal stability. The manufactured water-resistant composite films can be utilized as potential photonics materials, in particular for visualization of near-IR laser radiation and luminescent labels.

**Keywords:** cellulose nanocrystals, cellulose nanofibrils, nanocomposites, hydrophobicity, acrylic resins, SrF<sub>2</sub>:Ho, CaF<sub>2</sub>:Ho, up-conversion luminescence films.

Received: 1 October 2019

Revised: 4 October 2019

### 1. Introduction

Luminescent composite materials based on a nanocellulose matrix have attracted much attention due to environmental problems [1, 2] and their promising for photonics [3–7], optoelectronics [8–11], and biomedicine [12, 13]. Luminescent nanocomposites with a nanocellulose matrix are light-weight, flexible, thin materials with sufficient mechanical strength. These nanocomposites can be used in a number of practical applications, including: miniature biosensors and chemosensors [12–20], photodetectors [21, 22], organic light-emitting diodes [23, 24], organic solar cells [25], anti-counterfeiting [26] and different photonics devices [27–29].

Cellulose is a widely-spread natural “green” environmentally friendly polysaccharide, which has an amorphous-crystalline structure. Cellulose nanocrystals (CNC) and cellulose nanofibrils (CNF) are synthesized from wood and other plant sources, which have nanoscale transverse sizes and lengths ranging from nanometers to micrometers [30–32]. The preparation and properties of CNF and CNC are described in detail in numerous review articles [33–36]. Nanocellulose is a unique platform for nanocomposites producing due to attractive properties such as renewability, affordability, low density, unique optical properties, excellent mechanical properties, biocompatibility, and biodegradability. The properties of CNC and CNF make them promising for smart photonic devices [7, 37]. Thin CNC films are one-dimensional photonic crystals [38–40]. Like CNC, the CNF can form optically transparent films [41, 42]. One of the most specific nanocellulose characteristics is the presence of three free hydroxyl groups in each monomer unit, which provide a chemically active surface. A large number of hydroxyl groups on the nanocellulose surface is responsible for its inherent hydrophilic nature and possibilities for their modifications [1, 3, 33, 36].

CNF and CNC can serve as a matrix for inorganic phosphors. So Miao et al. developed a simple method for highly-transparent luminescent nanopaper production with high heat resistance by grafting Eu, Sm, Tb lanthanide complexes onto TEMPO-oxidized CNF [43]. Chu with co-authors synthesized chiral nematic CNC luminescent films with YVO<sub>4</sub>:Eu<sup>3+</sup> nanoparticles [44]. Yb (III) doped carbon quantum dots (CQD) grafted oxidized nanofibrillated cellulose (Yb<sup>3+</sup>-CQDs-ONFC) was proposed as novel anti-counterfeiting materials. The CQD serve as a visible emitter and antenna for the Yb<sup>3+</sup> ions NIR emission sensitizing. As a result, Yb<sup>3+</sup>-nanopaper fabricated from Yb<sup>3+</sup>-CQDs grafted ONFC by amide condensation show in eight times higher NIR emission than Yb<sup>3+</sup>-CQDs in solution with significant aggregation. Further, polystyrene as surface sizing was used to improve the water-resistant property in those nanopapers [45]. Nguyen with co-authors proposed to use nanocellulose as a matrix for up-conversion photonic

films production with chiral nematic ordering containing NaYF<sub>4</sub>: Yb,Er hexagonal nanorods [46]. Films have a low resistance to water due to the hydrophilic nature of the cellulose. The hydrophilic nature limits their using as luminescent composite materials based on CNF and CNC. Increase of hydrophobicity by surface modification is very attractive for manufacture of luminescent composite materials based on a nanocellulose matrix. The purpose of the modification is to change only the surface of the nanocellulose with preservation of the initial morphology of the nanocomposite material and the complex structure of internal hydroxyl groups.

This paper is devoted to the studies of hydrophobic composite luminescent nanocellulose films with up-conversion particles based on calcium and strontium fluorides doped with holmium for identify the hydrophobic agent influence on the change in the optical and luminescent properties of nanocomposite films.

## 2. Experimental section

### 2.1. Chemicals

Powdered bleached woodkraft cellulose (PCC-0.25 (PC) from Polycell, Vladimir, Russia), filter paper "Blue Ribbon" (FP), 98 % sulfuric acid, 18 % hydrochloric acid, double distilled water, acrylic varnish (KUDOKU-9002 from Elf Filling, Electrougli, Russia), regenerated cellulose dialysis tubing with 12 – 14 kDa molecular weight cut-off from Orange Scientific (Graigette Business Park, Braine-l'Alleud, Belgium), up-conversion Ca<sub>0.92</sub>Ho<sub>0.08</sub>F<sub>2.08</sub> and Sr<sub>1-x</sub>Ho<sub>x</sub>F<sub>2+x</sub> ( $x = 0.08$ , and  $0.10$ ) powders, which prepared by our proposed technique [47, 48] were used as starting materials.

### 2.2. Preparation techniques of cellulose nanocrystals and nanofibrills, and nanocellulose films

Initial PC cellulose samples were mixed with double distilled water (cellulose: H<sub>2</sub>O = 1:10 g/g) in a beaker. The prepared suspension was placed in an ice bath. Concentrated sulfuric acid (cellulose: H<sub>2</sub>SO<sub>4</sub> = 1:25 g/g) was added drop-wise to the cellulose suspensions under vigorous stirring until acid concentration reached about 65 wt%. The resulting suspension was placed in a water bath at 47 °C for 60 min under 350 rpm stirring. Hydrolysis was terminated by addition of 10-fold excess of cold double distilled water. The hydrolyzed suspension was washed with double distilled water and repeatedly centrifuged (Eppendorf 5804 centrifuge, 8000 rpm, 10 min). The supernatant was separated from the precipitate and then a new portion of water was added. After 4 – 5 centrifugation cycles, washing procedure was terminated at pH = 5. The resulting cellulose gel was dispersed in double distilled water and then placed into a dialysis bag and dialyzed for 7 days. After dialysis, the dispersion was sonicated for 15 min (UZG13-01/22 sonicator, 110 W, VNIITVCH) in an ice bath. The yield of CNC was about 30 %. The CNC content in the dispersion was determined gravimetrically. CNF was obtained by hydrolysis of FP with hydrochloric acid with followed by ultrasonic treatment. FP was preliminarily shredded into small pieces (2 × 2 mm). The aqueous suspension was prepared at FP:H<sub>2</sub>O = 1:10 g/g. Hydrochloric acid (FP:HCl = 1:13 g/g) was added drop-wise to the suspension under vigorous stirring at 80 °C for 20 min. The hydrolysis was terminated by adding a large amount of cold double distilled water (10 times the volume of the suspension). Further, the suspension was washed with double distilled water and repeatedly centrifuged (10 min at 8000 rpm, an Eppendorf 5804 centrifuge). The supernatant was separated from the precipitate and then a new portion of water was added. After 4 – 5 centrifugation cycles, washing was terminated at pH 4.5 – 5.0. The resulting cellulose gel was dispersed in double distilled water and sonicated in an ice bath for 15 min, then placed into a dialysis bag and dialyzed for 7 days. After dialysis, the suspension was sonicated according to the above-mentioned procedure. pH value was reached 5.5. The yield of CNF was about 50 %. The CNF content in the dispersion was determined gravimetrically. The resulting CNC and CNF dispersions were stored in a refrigerator at a temperature < 5 °C.

The nanocellulose films were prepared by solution casting technique of CNC, CNF dispersion with concentration less 3 wt.% in polystyrene Petri dishes with followed drying at ambient temperature for 2 – 3 days. The film thickness was about 25 – 35 μm.

### 2.3. Preparation of nanocomposites films

Ca<sub>0.92</sub>Ho<sub>0.08</sub>F<sub>2.08</sub> and Sr<sub>1-x</sub>Ho<sub>x</sub>F<sub>2+x</sub> ( $x = 0.08$  and  $0.10$ ) powders annealed at 750 °C were carefully ground in an agate mortar. The ground powders were dispersed in CNC or CNF colloidal solutions by sonication on an ice bath for 15 min. The colloidal suspensions were poured into polystyrene Petri dishes and dried under ambient conditions for 2 – 3 days. The air-dried composite films were further dried at 90 °C for 40 min to remove residual moisture, so that hydration would not affect the products' morphology, physical and luminescent characteristics. The film thickness was about 25 – 45 μm. The nanocellulose content in the dried films varied from 45 to 90 wt%, while the Ho content in the dried films ranged from 1.00 to 6.71 wt% for SrF<sub>2</sub>:Ho samples and from 2 to 8 wt.% for CaF<sub>2</sub>: Ho samples. The composite films were designated as CNC:xHo, CNF:xHo, CNC/CNF:xHo, where  $x = \text{Ho wt\%}$ .

## 2.4. Surface modification of nanocomposite films by acrylic resin

The hydrophobicity was reached by the simple procedure for applying a double-sided coating of KUDOKU-9002 acrylic varnish, which includes modified acrylic resin (ACR). Procedure consists of acrylic resin spraying from a balloon from 25 – 30 cm distance onto suspended composite films CNC:xHo, CNF:xHo, CNC/CNF:xHo. One to three thin layers were applied to each side of the film. The drying time between layers spraying was 5 – 10 minutes, then the next layer was applied. Dry to stick 20 – 30 minutes, but complete drying in air for 2 hours. The film thickness varied in the range of 45 – 75 μm, the thickness of the ACR layer was from 2.5 to 16 μm on each side. Designation of CNC composite films were CNC:xHo-zACR, CNF:xHo-zACR, CNC/CNF:xHo-zACR, where z is the number of layers deposited, from 1 to 3.

## 2.5. Characterization techniques and equipments

X-ray diffraction analysis was carried out on a Bruker D8 Advance diffractometer (Bruker AXS GmbH, Karlsruhe, Germany) using CuK $\alpha$ -radiation in the range 8 – 60 2 $\theta$  with 0.02 2 $\theta$  step. The diffraction peak at 22.7 2 $\theta$  was used for crystallinity index (IC, %) calculation by Segal's method according to Eq. (1):

$$IC = \frac{I_{200} - I_{AM}}{I_{200}} \times 100, \quad (1)$$

where,  $I_{200}$  is the intensity of the  $\langle 200 \rangle$  reflex at 22.70 2 $\theta$ .  $I_{200}$  consist of both crystalline and amorphous phases.  $I_{AM}$  is the intensity at the minimum between the  $\langle 200 \rangle$  and  $\langle 110 \rangle$  peaks at 18.00 2 $\theta$ .

The nanoparticle size distribution in aqueous dispersions was determined by dynamic light scattering (DLS) using a Photocor Complex DLS spectrometer equipped with He–Ne laser. The CNC and CNF dispersions were preliminarily diluted up to 0.01 wt% concentration and then sonicated for 5 min in an ice bath.

The degree of polymerization (DP) was measured by the viscosity method using diluted solutions of dry cellulose particles in Cadoxen (cadmium ethylenediamine) [49]. The polymerization degree was determined as the average of two independent measurements. The relative error was 4 % at  $p = 0.95$ .

Film thickness was measured using a micrometer (MKTS-25 0.001, Kalibron, Russia) at seven randomly selected locations on each film, and mean value was reported for each replication.

Water absorption test carried out for ACR film and without ACR layer nanocomposite films without ACR coatings were dried at 90 °C for 40 min and immersed in distilled water for 2 min. ACR coated nanocomposite films were immersed in distilled water for 2 min without drying. After immersed in doubly-distilled water, the samples were wet with FP to carefully remove excess water from the surface and weighed. Water adsorption % (WA) was calculated by the formula:

$$WA = \frac{W_{wet} - W_{dry}}{W_{dry}} \times 100, \quad (2)$$

where  $W_{dry}$  is the weight of the dried sample,  $W_{wet}$  is the weight of the wet sample after soaked in water for 2 min.

The microstructure of the particles in films was analyzed by scanning electron microscopy (SEM) using a NVision 40 microscope (Carl Zeiss NTS GmbH, Oberkochen, Germany) with simultaneous energy-dispersive spectroscopy (EDX) (X-Max detector, Oxford Instruments, Abingdon, UK).

Fourier transform infrared spectroscopy (FTIR) with ATR unit (Pike) was performed on a INFRALUM FT-08 spectrometer from 400 to 4000 cm<sup>-1</sup>. The transmission spectra were recorded using a Cary 5000 spectrophotometer in the 250 – 3000 nm range.

Thermal gravimetric analysis (TG) was performed from 25 to 800 °C with a 5 °C/min heating rate in air on the Netzsch TG 209 F1 Libra.

The contact angle was measured using the FTA1000 Drop Shape Instrument B Frame System. The test sample was placed on a horizontal holder. The water was applied to the surface of the test sample by a special microdosing syringe. The droplet volume was 100 μl. The image was recorded using a CCD detector of 640 × 480 pixels. Images were obtained 1 s after application of the droplets. The measurements were carried out at room temperature (24 ± 2 °C) and repeated 5 times on various fresh surfaces.

The up-conversion luminescence spectra were recorded with a Horiba FHR 1000 spectrophotometer with OL IS-670-LED integrating sphere (Gooch & Housego). A continuous solid-state LiYF<sub>4</sub>:Tm laser was used as the excitation source for Ho<sup>3+</sup> ions at 1912 nm. The beam diameter of incident laser radiation was 300 μm. The incident excitation power was 960 mW.

### 3. Results and discussion

#### 3.1. Characterization of a hydrophobic agent (ACR)

Acrylic universal gloss varnish KU-9002 was chosen as a hydrophobic agent. It contains xylene, methyl acetate, butanol, propanol, and modified acrylic resin (ACR). ACR is ethylhexyl acrylate, methyl methacrylate and styrene copolymer. The varnish is transparent, colorless and insoluble in water. KU-9002 designed to create a protective coating for metal, wood, and plastic products. It allows the masking of surface defects without yellowing and provides resistance to mechanical stress and abrasion. ACR has excellent surface adhesion and high environmental resistance [50]. Hardening takes place quickly at room temperature. The first drying came unstuck is 20 – 30 minutes but complete drying in the air for 2 hours. ACR contains esters of acrylic and methacrylic acids, as well as a phenyl group. The phenyl group ACR can improve the water-resistance of the film after drying [51]. Negatively polarized oxygen atoms of the ACR ester group are able to form hydrogen bonds [52]. Hydrogen bonds with the hydroxyl groups of nanocellulose improve the bonding between the nanocellulose film and the ACR. It ensures the uniformity of the ACR film on the surface of the nanocellulose. Intra- and intermolecular hydrogen bonds play a decisive role in the formation of supramolecular structures that affect on the nanocellulose properties. As a result, cellulose chains are assembled into highly ordered structures [4]. A possible mechanism for the interaction of a nanocellulose film and ACR in composite materials is shown in Fig. 1.

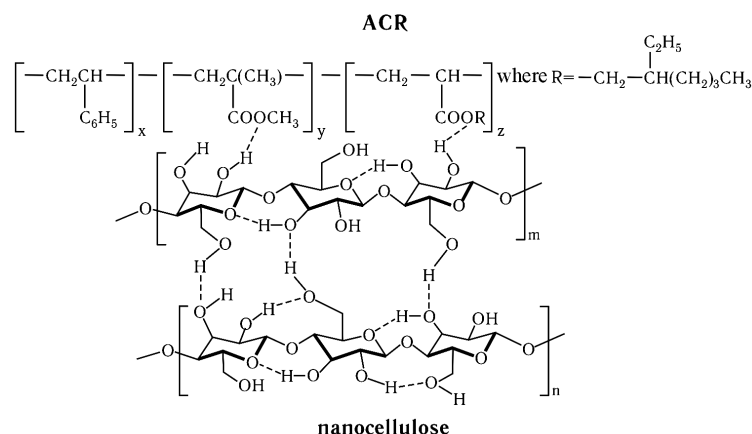


FIG. 1. Scheme of inter-surface hydrogen bonds between hydroxyl groups of nanocellulose and oxygen atoms of the ester group of ACR (ethylhexyl acrylate, methyl methacrylate and styrene copolymer)

#### 3.2. Characterization of dispersions, nanocellulose films, and nanocomposite films $\text{CaF}_2\text{:Ho}$ and $\text{SrF}_2\text{:Ho}$ with up-conversion particles

The 1.55 – 2.50 wt.% CNC aqueous dispersions are transparent and stable colloidal solutions of nanocrystalline cellulose, which staying without coagulation during for more than four months. The stability of CNC dispersions is explained by the presence of negatively charged sulfate groups on the surface of the CNC and an increase in the surface charge of CNC particles. It leads to a more stable CNC dispersion due to electrostatic repulsion between sulfate groups. The presence of sulfur in CNC samples (0.71 wt.%) confirmed by EDX analysis (Table 1) as a result of esterification of cellulose hydroxyl groups by sulfate ions.

Aqueous CNF dispersions with a concentration of 0.94 – 2.07 wt.% with milky hue are stable for a month. After one month of aging, the dispersion begins to stratify. Mixed aqueous dispersions of CNC/CNF with a concentration of 1.24 – 2.28 wt.% are transparent and stable colloidal solutions without coagulation for three months.

The hydrodynamic particle radii for CNC and CNF dispersion show a polydisperse particle distribution. CNC and CNF form whiskers and nanofibrils, respectively. Most particles are 10 – 30 nm and 90 – 170 nm sizes, but a small portion are aggregated CNCs. As a result of hydrolysis, the CNC particle sizes are reduced one thousand-fold compared to the initial PC. CNF is characterized by the presence of three groups of particles corresponding to sizes 22 – 32 nm, 90 – 180 nm, and 500 – 1800 nm.

Samples for SEM analysis were prepared by applying a drop of 0.01 wt.% dilute aqueous dispersions nanocellulose on the single-crystal silicon substrate with followed by drying in air. The properties of the initial cellulose (PC and FP) are shown in Table 2. Rod-like particles with a width of about 15 – 25 nm and length of about 100 – 200 nm,

TABLE 1. EDX analysis of nanocellulose

Elements	at. %		wt. %	
	CNC	CNF	CNC	CNF
C	53.8 ± 0.2	56.2 ± 0.1	46.5	49.1
O	45.8 ± 0.2	43.8 ± 0.1	52.8	50.9
S	0.3 ± 0.1	—	0.7	—

as well as aggregates are determined on SEM images for CNC samples (Fig. 2(a)). Cellulose nanofibrils with a width of 20 – 35 nm and length of 200 – 1800 nm with a large aspect ratio (ratio of length to smallest transverse size) of 20 – 60 are determined on SEM images for CNF films (Fig. 2(b)), which confirms the production of nanofibrillated cellulose. Nanocellulose prepared from a mixed dispersion of CNC/CNF = 1/1 present on Fig. 2(c,d). Entangled CNF fibrils form a porous network with CNC evenly distributed inside the CNF.

TABLE 2. Properties of the initial and synthesized nanocellulose

Sample	Particle size (SEM), nm		Cellulose Type Structure	IC, %	DP	Decomposition temperature
	diameter	length				$T_{onset}/T_{endset}, ^\circ\text{C}$
PC	25 – 50 *	230 – 500 *	IB	69.2	930	300/491
FP	25 – 50 *	200 – 1500 *	IB	68.7	1112	300/486
CNC	15 – 25	100 – 200	IB	86.2	105	157/567
CNF	22 – 35	200 – 1800	IB	70.3	154	196/591
CNC/CNF	15 – 35	100 – 1800	IB	71.6	147	186/567

\* Particle sizes of PC and FP are expressed in microns [53].

Particle sizes determined using SEM are consistent with DLS results.

CNC and CNF showed different behaviors during the film formation process due to the different shapes and lengths. CNCs tend to form the ordered structure, which associated with the self-assembly of CNC during slow drying. CNC forms transparent but fragile films. At 0.94 wt.% CNF dispersion, the flexible but wrinkled film with a milky tint is formed with porous network. The non-transparent film is formed at 2.07 wt.% dispersion concentration. In our earlier study of nanocellulose films was shown [53], that a transparent and flexible film was synthesized from CNC/CNF = 1/1 mixed dispersions.

Changes in the supramolecular structure of cellulose during hydrolysis are characterized by X-ray diffraction of cast films, but the monoclinic crystal structure of  $I\beta$  cellulose is preserved for all nanocellulose films (Fig. 3).

X-ray diffraction patterns of the CNC (Fig. 3(a)) samples revealed the  $I\beta$  crystal structure [54]. The CNC samples are characterized by a significant increase in the crystallinity index compared to the initial cellulose (Table 2) due to optimized acid hydrolysis process. A smaller increase in IC for CNF is observed due to the partial destruction of the amorphous regions of cellulose (Table 2).

The degree of polymerization for cellulose materials after hydrolysis is significantly reduced, namely by 8-fold for CNC. Moreover, CNC has a degree of polymerization about 1.3-fold less than CNF.

The thermal degradation of the initial cellulose (PC and FB) and nanocellulose (CNC and CNF) showed obvious differences (Table 2) [53]. Degradation onset temperature ( $T_{onset}$ ) in comparison to the initial cellulose was decreased by 100 and 140 °C for CNF and CNC, respectively. The decrease in thermal stability of CNC and CNF compared to the initial cellulose is probably associated with an increase of heat transfer rate due to an increase in surface area of smaller particle sizes. Also, it's probably due to the introduction of sulfate groups during acid hydrolysis. The lower temperatures of the  $T_{onset}$  (157 °C) for CNC compared to CNF/CNC (186 °C) are due to the higher content of sulfate

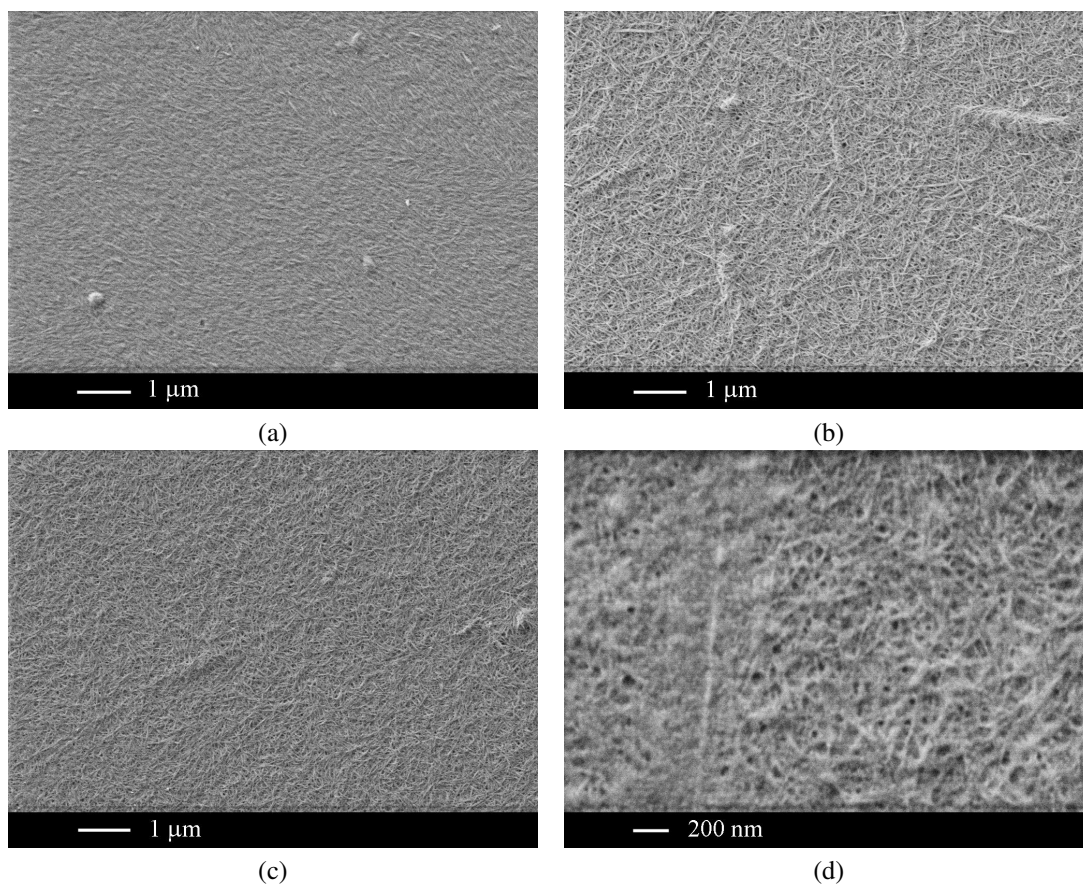


FIG. 2. SEM images of CNC and CNF: (a) CNC; (b) CNF; (c), (d) CNC/CNF

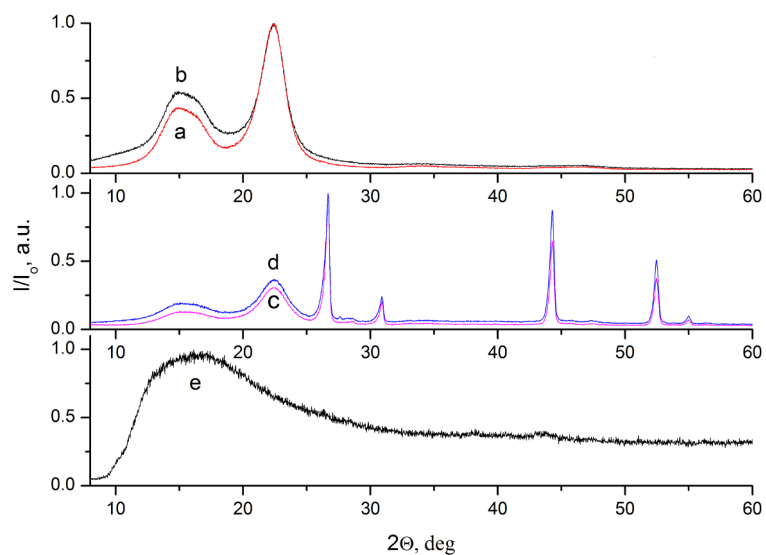


FIG. 3. X-ray pattern diffractions (a) CNC; (b) CNC-2ACR; (c) CNC: 5.5 Ho; (d) CNC: 5.5 Ho-1ACR; (e) ACR

groups in them, which is confirmed by EDX data. The total mass loss for all samples during thermal decomposition in the air is 100 %.

Finally, the morphology, particle size, the ratio of geometric parameters (sides), the degree of polymerization and the degree of crystallinity of nanocellulose are determined by preparation technique. Various mechanisms for the formation of CNC, CNF films affect their optical, thermal and mechanical properties.

Mixing CNC or CNC/CNF with Ca<sub>0.92</sub>Ho<sub>0.08</sub>F<sub>2.08</sub> particles, or Sr<sub>0.92</sub>Ho<sub>0.08</sub>F<sub>2.08</sub>, or Sr<sub>0.90</sub>Ho<sub>0.10</sub>F<sub>2.10</sub> particles with the subsequent ultrasonic treatment result in good distribution of the filler in the nanocellulose matrix. The resulting dispersion is transparent and stable during the day with 0.28 – 1.57 wt.% content of up-conversion powders.

The X-ray diffraction pattern of the CNC: 5.5Ho (45.4 wt% Sr<sub>0.90</sub>Ho<sub>0.10</sub>F<sub>2.10</sub>) composite film exhibit diffraction peaks characteristic of cellulose *Iβ* and the crystalline fluorite phase Sr<sub>0.90</sub>Ho<sub>0.10</sub>F<sub>2.10</sub> with unit cell parameter *a* = 5.7778(1) Å (Fig. 3(c)).

It means that the crystalline structure of cellulose does not change after dispersion since the positions of all reflexes are preserved but their intensity changes.

The thermal destruction of CNC: 4.4Ho composite film (36.4 wt.% Sr<sub>0.90</sub>Ho<sub>0.10</sub>F<sub>2.10</sub>) begins in the air at 157 °C (Fig. 4(b)). The latter does not differ from the decomposition temperature of CNC film (Table 2). According to TG, the residue after heating up to 800 °C is 36.4 wt.%, which corresponds to the content of up-conversion powder in the composite film.

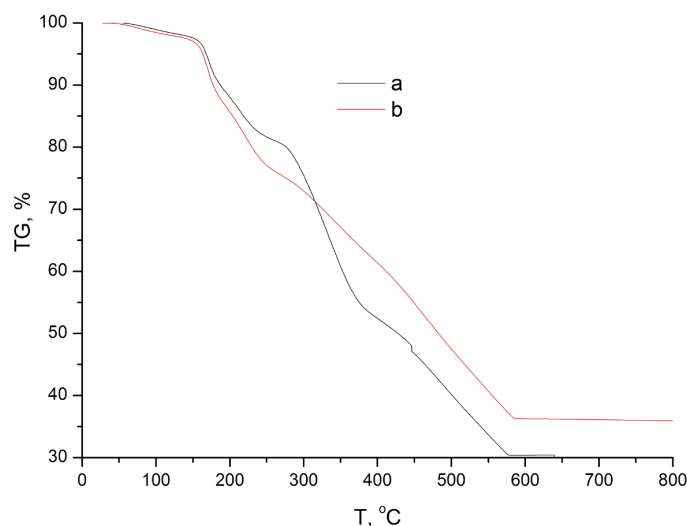


FIG. 4. TG measurements in the air at a heating rate of 5 °/min for films: (a) CNC: 4.4 Ho-1ACR; (b) CNC: 4.4 Ho

Scanning electron microscopy images of the surface and cleavage of composite films CNC/CNF: 4.6Ho (37.7 wt.% Sr<sub>0.90</sub>Ho<sub>0.10</sub>F<sub>2.10</sub>) and CNC: 5.1Ho (34.8 wt.% Ca<sub>0.92</sub>Ho<sub>0.08</sub>F<sub>2.08</sub>) analyzed in topographic contrast (Fig. 5(a, c, e, g)) and in the Z contrast (Fig. 5(b, d, f, h)).

CNC/CNF: 4.6Ho and CNC: 5.1Ho composite films have a uniform morphology and contain uniformly distributed up-conversion particles over the entire surface and volume (Fig. 5(c, d, f, h)). The SrF<sub>2</sub>:Ho and CaF<sub>2</sub>:Ho particle size varies between 50 – 200 nm. EDX analysis confirmed that the measured atomic ratio of Sr/Ho and Ca/Ho elements in composites is very close to that measured in Sr<sub>0.90</sub>Ho<sub>0.10</sub>F<sub>2.10</sub> and Ca<sub>0.92</sub>Ho<sub>0.08</sub>F<sub>2.08</sub> powders. Thus, the use of CNC or mixed CNC/CNF dispersions (1:1) allows to composite films producing with a uniform distribution of up-conversion particles without losses and changing of the crystal structure.

The thickness of composite films depends on the concentration and volume of CNC and CNC/CNF dispersions, as well as on the content of up-conversion particles in them. The optimal concentration of nanocellulose dispersions is 1.8 – 2.2 wt.% with the 0.9 – 1.3 wt.% content of up-conversion particles for preparation of composite films with a thickness of 35 – 50 μm. Such concentrations ensure the stability of the dispersions and the drying of the film in during two days.

### 3.3. Effect of ACR coating on the thermal, structural, optical, and luminescent properties of composite films

The thermal stability of a CNC: 4.4Ho-1ACR composite ACR coated films do not change in comparison to uncoated film (Fig. 4(a)). An increase in losses during annealing by 6.3 % in comparison to CNC: 4.4Ho film is

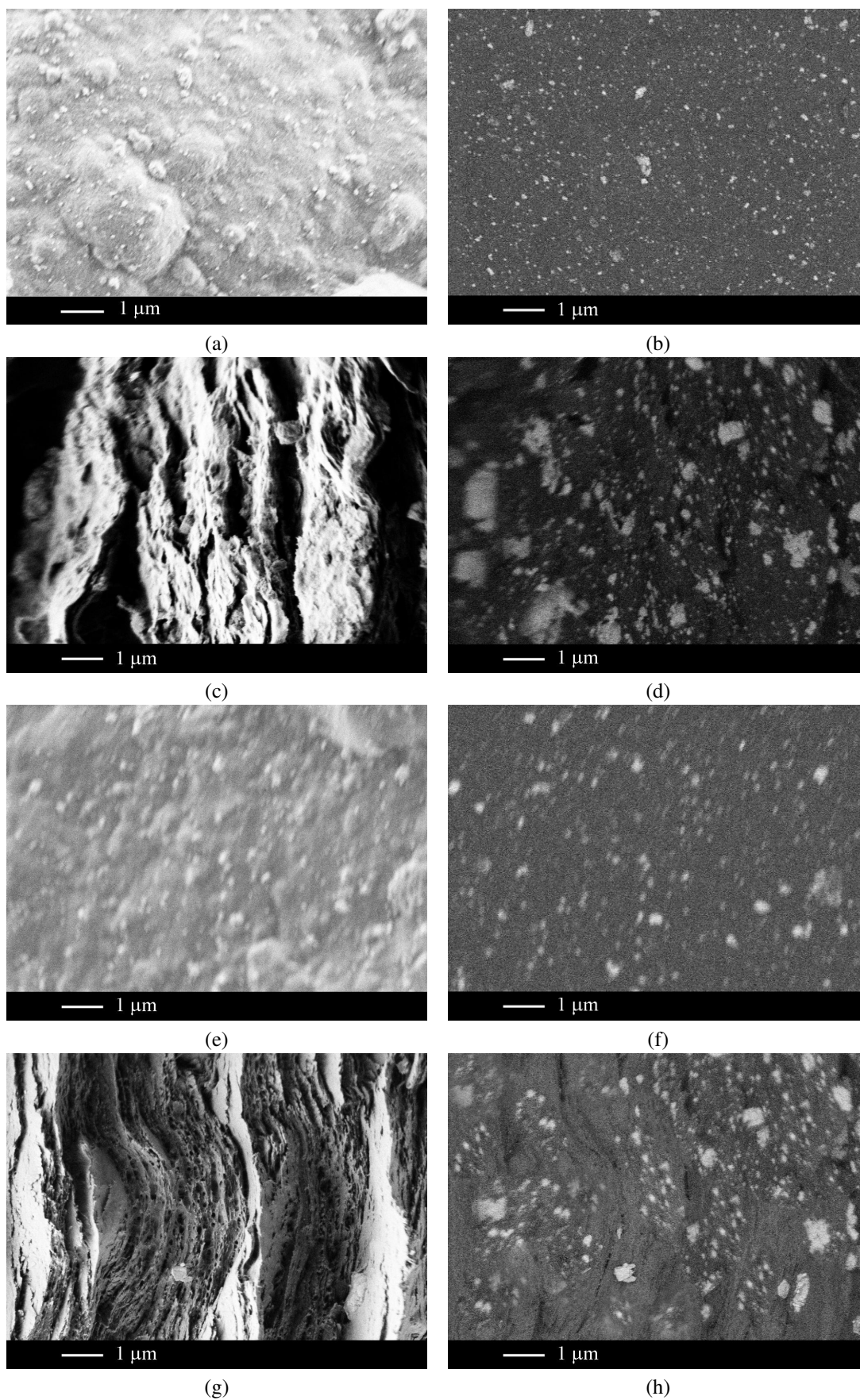


FIG. 5. SEM images of CNC/CNF film: 4.6 Ho (a, c) – in topographic contrast, (b, d) – in cleaved film Z-contrast, (c, d) – cross section of the film.. CNC: 5.1 Ho (e, g) – in topographic contrast, (f, h) – film cleavage in Z-contrast, (g, h) – cross section of the film

associated with the burnout of the ACR coating. It was found that the crystalline structure of nanocellulose does not change after applying the ACR coating since the positions of all reflections are preserved but intensity changes (Fig. 3(b,d)). An increase of the amorphous halo intensity is also noted, which can be explained by the amorphous nature of ACR coating. The X-ray diffraction pattern of the ACR film does not have clear reflections (Fig. 3(e)).

The IR spectrum of CNC films contains absorption bands about 2900 cm<sup>-1</sup> (stretching modes of the CH and CH<sub>2</sub> groups), about 1430 cm<sup>-1</sup> (symmetric deformation vibrations of the CH<sub>2</sub> group), 1000 – 1200 cm<sup>-1</sup> (stretching vibrations of C–O–C and C–O bonds in the pyranose ring) (Fig. 6(a)). The CNC spectrum has a weak band at 1203 cm<sup>-1</sup> (S = O), which confirms the introduction of a sulfate group into the cellulose structure during acid hydrolysis [55].

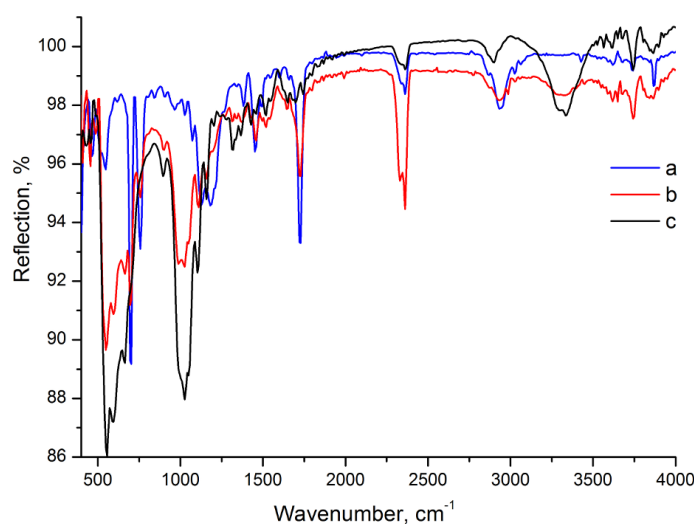


FIG. 6. IR spectra of (a) ACR, CNC-ACR (b), and (c) CNC films

The spectrum for CNC is characterized by a wide absorption band in the region 3284 – 3335 cm<sup>-1</sup> (stretching modes of hydroxyl groups included in the hydrogen bond). In the IR spectrum of the ACR film, wide bands at 2868, 2933 and 2951 cm<sup>-1</sup> are caused by aliphatic regions (C–H), such as CH<sub>2</sub> and CH<sub>3</sub> (Fig. 6(a)). Absorption spectrum contains band at 1725 cm<sup>-1</sup> (stretching vibrations of the C=O ester group), at 1128 and 1183 cm<sup>-1</sup> (stretching vibrations of C–O groups), and at 1452 and 1340 cm<sup>-1</sup> (symmetric and asymmetric stretching vibrations of C–CH<sub>3</sub>). The absorption band at 698 and 756 cm<sup>-1</sup> are associated with the out-of-plane transverse vibrations of the phenyl ring and out-of-plane peak CH, respectively [56]. The shape of the complicated peak at 3273 – 3356 cm<sup>-1</sup> for the CNC-ACR film becomes wider and shifts along compared to pure CNC. It can be explained by the formation of inter-surface hydrogen bonds between CNC hydroxyl groups and oxygen atoms in ACR ester group. It confirmed by the shift of the bands of C–O groups to 1108 and 1157 cm<sup>-1</sup> (Fig. 6).

A comparison of the transmittance spectra of the same composition films with ACR coating (Fig. 7(a, c, d)) and without coating (Fig. 7(b, e, f)) confirms that the transparency of films with ACR coating significantly (by 20 – 25 %) improves in the visible and near IR spectral regions.

Comparison of the SEM images of the CNC: 5.1Ho (34.8 wt.% Ca<sub>0.92</sub>Ho<sub>0.08</sub>F<sub>2.08</sub>) surface without coating (Fig. 8(a)) and with ACR coating shows that the coating of the transparent acrylic resin provides good surface smoothness. ACR fills all of the irregularities of the composite films (Fig. 8(b)), which resulted in increase in the transparency of composite films with ACR coating. However, the uniformity of the coating depended on the thickness of the ACR layer. The triple-layer coating resulted in cracks on the film (Figs. 8(c, d)), which did not affect on the optical transmission but reduced the water-resistance of the films (Table 3).

Films of CNC/CNF: 4.6Ho (37.7 wt.% Sr<sub>0.90</sub>Ho<sub>0.10</sub>F<sub>2.10</sub>) (Fig. 9(a)) and CNC/CNF: 4.6Ho-2ACR (Fig. 9(b)) are flexible, uniform, and wrinkle-free. The film without ACR is translucent, while the film with ACR is almost transparent.

The luminescence intensity of composite films with ACR coating (CNC/CNF: 8.4Ho-2ACR, CNC/CNF: 6.8Ho-2ACR) is higher than films without ACR coating (CNC/CNF: 8.4Ho (57.5 wt.% Ca<sub>0.92</sub>Ho<sub>0.08</sub>F<sub>2.08</sub>), CNC/CNF: 6.8Ho (55.8 wt.% Sr<sub>0.90</sub>Ho<sub>0.10</sub>F<sub>2.10</sub>)) with the same amount of holmium (Fig. 10). The ACR coating protects the nanocomposite film from atmospheric moisture and prevents luminescence quenching.

Finally, it was determined that the ACR coating improves the optical transmission and luminescent properties of up-conversion nanocomposite films based on nanocellulose.

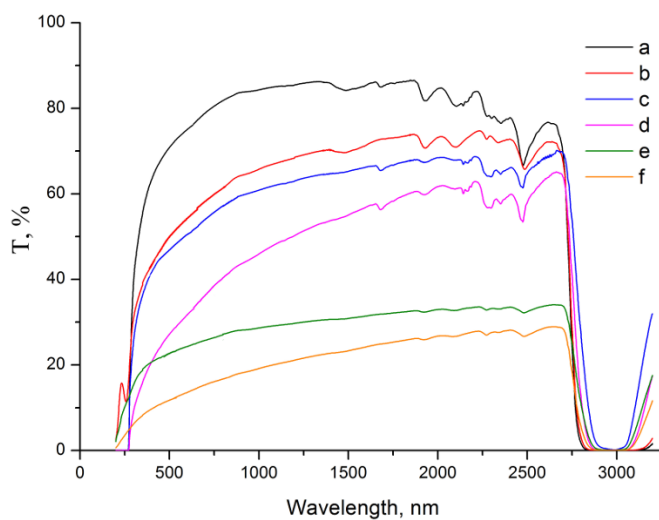


FIG. 7. Transmission spectra of films: a) CNC/CNF-2ACR; (b) CNC/CNF; (c) CNC: 5.4 Ho-2ACR; (d) CNC/CNF: 6.8 Ho-2ACR; (e) CNC: 5.4 Ho (54.5 wt.%  $\text{Sr}_{0.92}\text{Ho}_{0.08}\text{F}_{2.08}$ ); (f) CNC/CNF: 6.8 Ho (55.8 wt.%  $\text{Sr}_{0.90}\text{Ho}_{0.10}\text{F}_{2.10}$ )

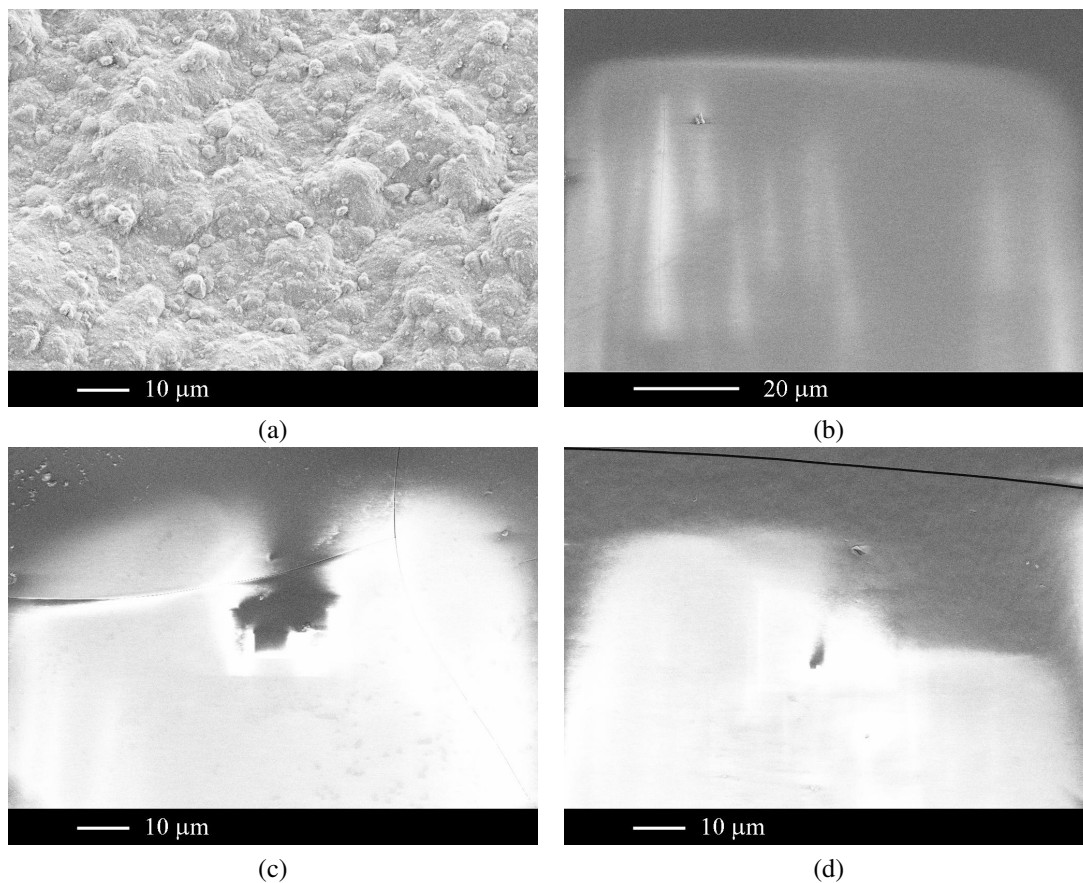
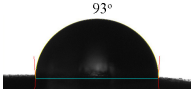
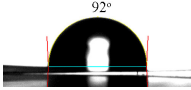


FIG. 8. SEM images of film surface: (a) CNC: 5.1 Ho; (b) CNC: 5.1 Ho-2ACR; (c, d) CNC: 5.1 Ho-3ACR

TABLE 3. Wetting angle and water adsorption of nanocomposite films with different number of applied acrylic resin layers

Film composition	Film thickness, $\mu\text{m}$	ACR, wt. %	WA, wt. %	Wetting angle
CNC/CNF: 4.6 Ho (37.7 wt.% Sr <sub>0.90</sub> Ho <sub>0.10</sub> F <sub>2.10</sub> )	50 ± 2	—	46.8	14° 
CNC/CNF: 4.6 Ho-1ACR (37.7 wt.% Sr <sub>0.90</sub> Ho <sub>0.10</sub> F <sub>2.10</sub> )	59 ± 2	9.8	0	93° 
CNC: 5.1 Ho (57.5 wt.% C <sub>0.92</sub> Ho <sub>0.08</sub> F <sub>2.08</sub> )	42 ± 2	—	53.0	0° 
CNC: 5.1 Ho-2ACR (57.5 wt.% C <sub>0.92</sub> Ho <sub>0.08</sub> F <sub>2.08</sub> )	58 ± 2	21.5	0	100° 
CNC: 5.1 Ho (57.5 wt.% C <sub>0.92</sub> Ho <sub>0.08</sub> F <sub>2.08</sub> )	35 ± 2	—	53.3	0° 
CNC: 5.1 Ho-3ACR (57.5 wt.% C <sub>0.92</sub> Ho <sub>0.08</sub> F <sub>2.08</sub> )	65 ± 2	48.3	6.1	92° 



(a)



(b)

FIG. 9. Film photos: (a) CNC/CNF: 4.6 Ho; (b) CNC/CNF: 4.6 Ho-2ACR

### 3.4. Effect of ACR coating thickness on the hydrophobic properties of composite films

The cleaved composite films with a different number of ACR coating layers demonstrate the strong adhesion of the ACR to the surface of the nanocellulose film (Fig. 11). This indicates a good interaction and compatibility of nanocellulose with ACR due to the presence of hydrogen bonds between the hydroxyl groups of CNC and oxygen atoms of ACR ester group, which is confirmed by IR spectra (Fig. 6). ACR layer thicknesses are 3 – 5  $\mu\text{m}$ , 7 – 10  $\mu\text{m}$  and 14 – 17 microns for single, double, and triple-layered coatings, respectively. Cracks appear in the ACR layer for the triple-layered coating (Fig. 11(d)), which are also visible on the film surface (Fig. 8(c, d)).

The use of ACR coatings provides an easy way to impart hydrophobic properties to nanocomposite films (Table 3).

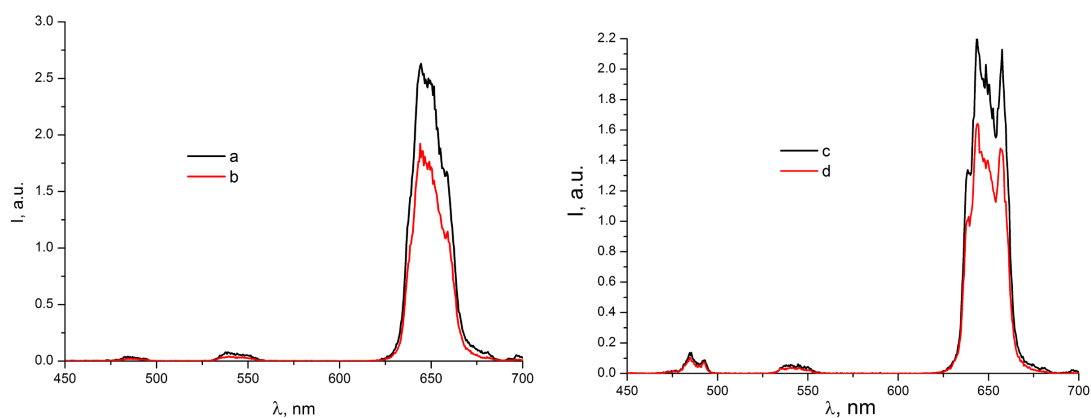


FIG. 10. Up-conversion luminescence spectra of composite films: (a) CNC/CNF: 8.4 Ho-2ACR; (b) CNC/CNF: 8.4 Ho; (c) CNC/CNF: 6.8 Ho-2ACR; (d) CNC/CNF: 6.8 Ho

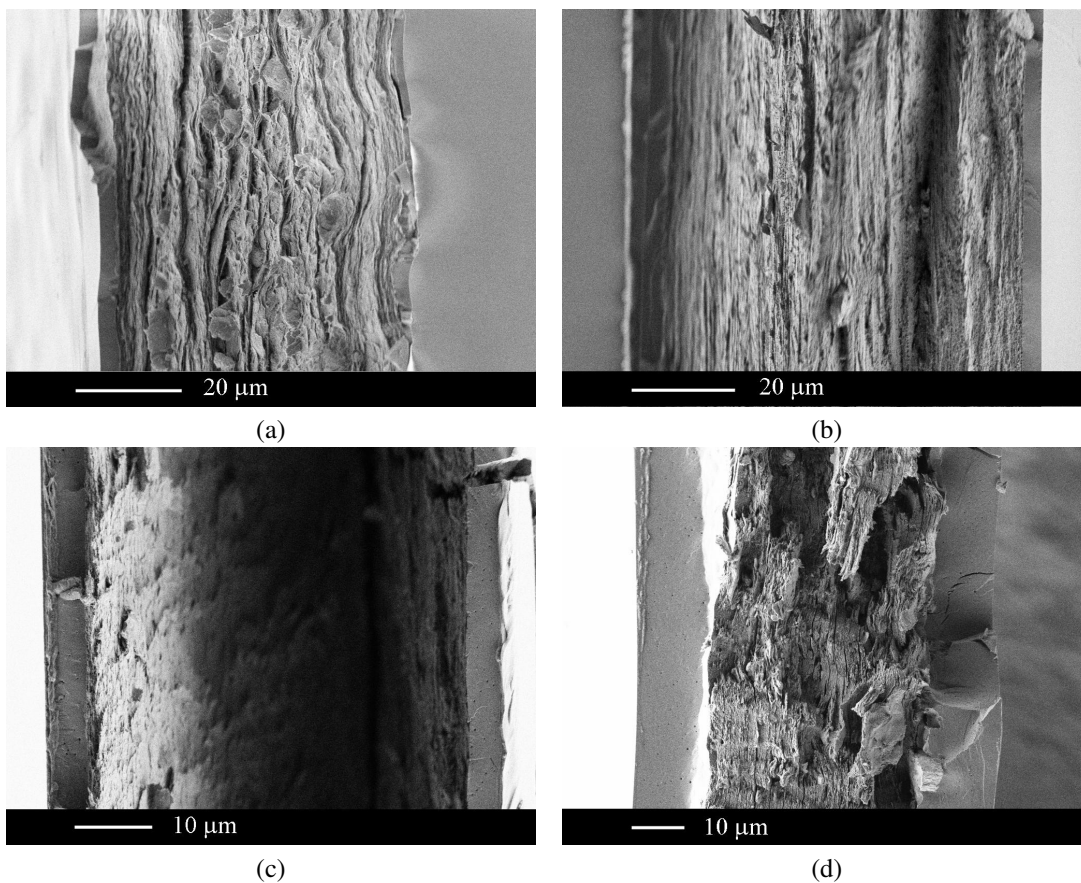


FIG. 11. SEM image of cleaved films: (a) CNC/CNF: 4.6 Ho-1ACR; (b) CNC/CNF-1ACR; (c) CNC: 5.1 Ho-2ACR; (d) CNC: 5.1 Ho-3ACR

The ACR uncoated nanocomposite film is hydrophilic and easily wetted by water. Water adsorption and water contact angle of CNC/CNF: 4.6 Ho and CNC: 5.1Ho films are 47 and 53 %, and 15 and 0°, respectively. After a single-layer ACR coating, the film acquired hydrophobic properties. This was confirmed by the water contact angle (93°) and the absence of water adsorption. After a two-layer coating of the film, the water contact angle increased up to 100° without water adsorption. Three-layer coating demonstrate the water contact angle (92°), but the water adsorption of the film was 6 %. This behavior is associated with a presence of cracks in the thick ACR layer. Water penetrates into the composite film via cracks. Studies have shown that a two-layer ACR coating with a layer thickness of 7 – 10 μm provides good hydrophobic properties of up-conversion composite films with simultaneously improving transparency and luminescent properties.

#### 4. Conclusions

By spraying a two-layer ACR coating with 7 – 10 μm thickness onto up-conversion CNC/CNF/MF<sub>2</sub>:Ho composite films, the hydrophobic composite films with a water contact angle of 100±2° and good water resistance were prepared. The water adsorption of up-conversion composite films after applying a two-layer ACR coating decreased from 53 to 0 %. The thickness effect of the ACR layer on the film water-resistance is established. After applying a three-layer ACR coating, the thickness of the ACR layer is approximately 14 – 17 μm with water adsorption increase. It associated with the presence of cracks in the ACR layer. Using TGA and X-ray diffraction, it was shown that the deposition of ACR coatings did not affect on the thermal stability of the films and the crystal structure of CNC, CNF, and up-conversion particles. SEM studies show strong adhesion of ACR to the surface of a nanocellulosic film. This indicates good adhesion and interaction of nanocellulose with ACR due to the presence of hydrogen bonds between hydroxyl groups in CNC/CNF and oxygen atoms of the ACR ester group. The transparent acrylic resin coating led to a smoother surface, which contributed to an increase in the transparency of composite films with ACR coating by 20 – 25 % in the visible and near-infrared spectral range with a simultaneous improvement in luminescent properties. Water-resistant, flexible, uniform, translucent up-conversion films with a thickness of 50 – 65 μm were prepared. These films can be used as a potential material for the photonics, as a luminescent label, luminescent detector, and in particular for imaging near-IR laser radiation, etc.

#### Acknowledgements

The study was funded by the Russian Foundation for Basic Research (RFBR 16-29-11784-ofi-m).

#### References

- [1] Thomas B., Raj M.C., et al. Nanocellulose, a Versatile Green Platform: From Biosources to Materials and Their Applications. *Chem. Rev.*, 2018, **118** (24), P. 11575–11625.
- [2] Eichhorn S.J., Rahatekar S.S., Vignolini S., Windle A.H. New horizons for cellulose nanotechnology. *Phil.Trans. R. Soc. A*, 2018, **376**, 20170200.
- [3] Kontturi E., Laaksonen P., et al. Advanced Materials through Assembly of Nanocelluloses. *Adv. Mater.*, 2018, **30**, 1703779.
- [4] Abitbol T., Rivkin A., et al. Nanocellulose, a tiny fiber with huge applications. *Curr. Opin. Biotechnol.*, 2016, **39**, P. 76–88.
- [5] Jiang H., Zhou D., et al. Self-organized helical superstructure of photonic cellulose loaded with upconversion nanoparticles showing modulated luminescence. *RSC Advances*, 2016, **6**, P. 76231–76236.
- [6] Xue B., Zhang Z., et al. Near-infrared emissive lanthanide hybridized nanobrillated cellulose nanopaper as ultraviolet lter. *Carbohydr. Polym.*, 2018, **186**, P. 176–183.
- [7] Eichhorn S.J. Cellulose Nanofibres for Photonics. *Curr. Opin. Green and Sustainable Chemistry*, 2018, **12**, P. 1–7.
- [8] Yu Z., Xu Z., et al. Water-Resistant and Haze-Tunable Transparent Cellulose Nanopaper for Patterned Electroluminescence Devices. *Macromol. Mater. Eng.*, 2018, **306** (6) 1800142.
- [9] Du X., Zhang Z., Liu W., Deng Y. Nanocellulose-based conductive materials and their emerging applications in energy devices – A review. *Nano Energy*, 2017, **35**, P. 299–320.
- [10] Vicente A.T., Araujo A., et al. Multifunctional cellulose-paper for light harvesting and smart sensing applications. *J. Mater. Chem. C*, 2018, **6**, P. 3143–3181.
- [11] Ha D., Fang Z., Zhitenev N.B. Paper in Electronic and Optoelectronic Devices. *Adv. Electron. Mater.*, 2018, **4** (5), 1700593.
- [12] Seabra A.B., Bernardes J.S., et al. Cellulose nanocrystals as carriers in medicine and their toxicities: A review. *Carbohydr. Polym.*, 2018, **181**, P. 514–527.
- [13] Yang J., Li J. Self-assembled cellulose materials for biomedicine: A review. *Carbohydr. Polym.*, 2018, **181**, P. 264–274.
- [14] Morales-Narváez E., Golmohammadi H., et al. Nanopaper as an Optical Sensing Platform. *ACS Nano*, 2015, **9**, P. 7296–7305.
- [15] Li M., Li X., Xiao H.N., James T.D. Fluorescence sensing with cellulose-based materials. *Chemistry Open*, 2017, **6**, P. 685–696.
- [16] Golmohammadi H., Morales-Narváez E., Naghdi T., Merkoj A. Nanocellulose in Sensing and Biosensing. *Chem. Mater.*, 2017, **29**, P. 5426–5446.
- [17] Zor E., Alpaydin S., et al. Photoluminescent nanopaper-based microcuvette for iodide detection in seawater. *Sens Actuators B Chem.* 2018, **254**, P. 1216–1224.
- [18] Dong S., Roman M. Fluorescently Labeled Cellulose Nanocrystals for Bioimaging Applications. *J. Am. Chem. Soc.*, 2007, **129**, P. 13810–13811.

- [19] Pouzesh M., Nekouei S., et al. Fabrication of stable copper nanoparticles embedded in nanocellulose film as a bionanocomposite plasmonic sensor and thereof for optical sensing of cyanide ion in water samples. *Cellulose*, 2019, **26** (8), P. 4945–4956.
- [20] Guan Q., Song R., et al. Fluorescent CdTe-QD-encoded nanocellulose microspheres by green spraying method. *Cellulose*, 2018, **25** (12), P. 7017–7029.
- [21] Yan C.-Y., Fang Z.-Q., et al. A tunable optoelectronic nanobrillated cellulose/CdS quantum dot film with improved transmittance and strength. *Cellulose*, 2018, **25**, P. 2405–2417.
- [22] Park J., Seo J.-H., et al. Flexible and Transparent Organic Phototransistors on Biodegradable Cellulose Nanofibrillated Fiber Substrates. *Adv. Optical Mater.*, 2018, **6** (9), 1701140.
- [23] Zhang Z., Zhang M., et al. Irreversible Solvatochromic Zn-Nanopaper Based on Zn(II) Terpyridine Assembly and Oxidized Nanofibrillated Cellulose. *ACS Sustainable Chem. Eng.*, 2018, **6**, 11614.
- [24] Yang S., Xie Q., et al. Acetylation improves thermal stability and transmittance in FOLED substrates based on nanocellulose films. *RSC Adv.*, 2018, **8**, P. 3619–3625.
- [25] You Y., Zhang H., et al. Preparation and properties of  $\text{Sr}_2\text{Si}_5\text{N}_8:\text{Eu}^{2+}$ -cellulose hybrid films for sunlight conversion. *Cellulose*, 2015, **22**, P. 3337–3345.
- [26] Zhang L., Lyu S., Chen Z., Wang S. Fabrication Flexible and Luminescent Nanofibrillated Cellulose Films with Modified  $\text{SrAl}_2\text{O}_4:\text{Eu}$ , Dy Phosphors via Nanoscale Silica and Aminosilane. *Nanomaterials*, 2018, **8**, 352.
- [27] Zhang L., Lyu S., et al. Dual-emitting film with cellulose nanocrystal-assisted carbon dots grafted  $\text{SrAl}_2\text{O}_4$ ,  $\text{Eu}^{2+}$ ,  $\text{Dy}^{3+}$  phosphors for temperature sensing. *Carbohydr. Polym.*, 2019, **206**, P. 767–777.
- [28] Zor E. Silver nanoparticles-embedded nanopaper as a colorimetric chiral sensing platform. *Talanta*, 2018, **184**, P. 149–155.
- [29] Querejeta-Fernández A., Chauve G., et al. Chiral Plasmonic Films Formed by Gold Nanorods and Cellulose Nanocrystals. *J. Am. Chem. Soc.*, 2014, **136**, P. 4788–4793.
- [30] Klemm D., Heublein B., Fink H.-P., Bohn A. Cellulose: fascinating biopolymer and sustainable raw material. *Angew Chem. Int. Edit.*, 2005, **44**, P. 3358–3393.
- [31] Habibi Y., Lucia L.A., Rojas O.J. Cellulose nanocrystals: chemistry, self-assembly, and applications. *Chem. Rev.*, 2010, **110**, P. 3479–3500.
- [32] Klemm D., Kramer F., et al. Nanocelluloses: a new family of nature-based materials: a review. *Angew Chem. Int. Edit.*, 2011, **50**, P. 5438–5466.
- [33] Foster E.J., Moon R.J., et al. Current characterization methods for cellulose nanomaterials. *Chem. Soc. Rev.*, 2018, **47**, P. 2609–2679.
- [34] Jonoobi M., Oladi R., et al. Different preparation methods and properties of nanostructured cellulose from various natural resources and residues: a review. *Cellulose*, 2015, **22**, P. 935–969.
- [35] Mondal S. Preparation, properties and applications of nanocellulosic materials. *Carbohydr. Polym.*, 2017, **163**, P. 301–316.
- [36] Kargarzadeh H., Mariano M., et al. Advances in cellulose nanomaterials. *Cellulose*, 2018, **25**, P. 2151–2189.
- [37] Hamad W.Y. Cellulose Nanocrystals and Nanofibrils in Advanced Applications, in *Handbook of Nanocellulose and Cellulose Nanocomposites* (eds H. Kargarzadeh, I. Ahmad, S. Thomas and A. Dufresne), Wiley-VCH Verlag GmbH & Co. KGaA, Weinheim, Germany, 2017, P. 799–829.
- [38] Wilts B.D., Dumanli A.G., et al. Chiral optics of helicoidal cellulose nanocrystal lms. *APL Photonics*, 2017, **2**, 040801.
- [39] Gray D.G. Recent advances in chiral nematic structure and iridescent color of cellulose nanocrystal lms. *Nanomaterials*, 2016, **6**, 213.
- [40] Surov O.V., Voronova M.I., Zakharov A.G. Functional materials based on nanocrystalline cellulose. *Russ. Chem. Rev.*, 2017, **86**, P. 907–933.
- [41] Qing Y., Sabo R., et al. Self-assembled optically transparent cellulose nanofibril films: effect of nanofibril morphology and drying procedure. *Cellulose*, 2015, **22**, P. 1091–1102.
- [42] Sun X. Wu Q., et al. Nanocellulose films with combined cellulose nanofibers and nanocrystals: tailored thermal, optical and mechanical properties. *Cellulose*, 2018, **25**, P. 1103–1115.
- [43] Miao M., Zhao J., et al. Fast fabrication of transparent and multi-luminescent TEMPO-oxidized nanofibrillated cellulose nanopaper functionalized with lanthanide complexes. *J. Mater. Chem. C*, 2015, **3**, P. 2511–2517.
- [44] Chu G., Wang X., et al. Chiral electronic transitions of  $\text{YVO}_4:\text{Eu}^{3+}$  nanoparticles in cellulose based photonic materials with circularly polarized excitation. *J. Mater. Chem. C*, 2015, **3**, P. 3384–3390.
- [45] Nguyen T.D., Hamad W.Y., MacLachlan M.J. Near-IR sensitive up-converting nanostructured photonic cellulose films. *Adv. Opt. Mater.*, 2017, **5**, 1600514.
- [46] Zhang Z., Chang H., et al. Near-infrared and visible dual emissive transparent nanopaper based on Yb(III)-carbon quantum dots grafted oxidized nanofibrillated cellulose for anti-counterfeiting applications. *Cellulose*, 2018, **25** (1), P. 377–389.
- [47] Fedorov P.P., Luginina A.A., et al. Preparation of nanodispersed fluorite-type  $\text{Sr}_{1-x}\text{R}_x\text{F}_{2+x}$  (R = Er, Yb, Ho) phases from citrate solutions. *J. Fluorine Chem.*, 2017, **194**, P. 8–15.
- [48] Kuznetsov S.V., Proydakova V.Yu., et al. Synthesis and quantum yield investigations of the  $\text{Sr}_{1-x-y}\text{Pr}_x\text{Yb}_y\text{F}_{2+x+y}$  luminophores for photonics. *Nanosystems: Phys., Chem., Math.*, 2018, **9** (5), P. 663–668.
- [49] Ioelovich M.Y. Study of cellulose interaction with concentrated solutions of sulfuric acid. *ISRN Chem. Eng.*, 2012, 4289741.
- [50] Acrylic universal gloss varnish KU-9002. Technical Information Sheet. URL: <https://kudo-paint.ru/products/dekorativnaya-seriya/laki/lak-akrilovyj-universalnyj-glyantsevyy/>
- [51] Song X., Yang S., et al. Transparent and Water-Resistant Composites Prepared from Acrylic Resins ABPE-10 and Acetylated Nanofibrillated Cellulose as Flexible Organic Light-Emitting Device Substrate. *Nanomaterials*, 2018, **8** (9), 648.
- [52] Ternay A.L. *Contemporary Organic Chemistry*. W. B. Saunders Co, Philadelphia, 1976, 993.
- [53] Fedorov P.P., Luginina A.A., et al. Composite up-conversion luminescent films containing a nanocellulose and  $\text{SrF}_2:\text{Ho}$  particle. *Cellulose*, 2019, **26** (4), P. 2403–2423.
- [54] Feng X., Meng X., et al. Extraction and preparation of cellulose nanocrystals from dealginate kelp residue: structures and morphological characterization. *Cellulose*, 2015, **22**, P. 1763–1772.
- [55] Al-Dulaimi A.A., Wanrosli W. Isolation and Characterization of Nanocrystalline Cellulose from Totally Chlorine Free Oil Palm Empty Fruit Bunch Pulp. *J. Polym. Environ.*, 2017, **25**, P. 192–202.
- [56] Slepchuk I., Semeshko O.Ya., Asauljuk T.S., Saribekova Yu.G. Investigation of impact of crosslinking agents on characteristics of spatial net and properties of styrene-acrylic polymer films. *Izv. Vyssh. Uchebn. Zaved. Khim. Khim. Tekhnol.*, 2018, **61**(7), P. 68–76 (in Russian).